Pergamon

Int. J. Heat Mass Transfer. Vol. 38, No. 5, pp. 767–777, 1995

0017-9310/95 $9.50+0.00

0017-9310(94)00210-X

Forced convection from a surface covered with flexible fibers

ALEX J. FOWLER and ADRIAN BEJAN†

Department of Mechanical Engineering and Materials Science, Duke University, Durham, NC 27708-0300, U.S.A.

(*Received* 18 *April* 1994 *and in final form* 16 *July* 1994)

Abstract—The heat transfer, friction and mechanical (elastic) interaction between an external laminar flow and a solid surface covered by a layer of fibers is investigated numerically. The flow is initially perpendicular to the surface, and the fibers can bend. The study has two parts. In the first part it is assumed that the fibers are inflexible. It is shown that the effect of the fiber layer on the overall heat transfer can be correlated in terms of the fraction of the external flow that penetrates into the fiber layer. The second part focuses on the effect of fiber bending, which is described by a new dimensionless group: the stiffness number $S = EI/(\rho U_\infty^2 L^4)$. It is shown that the wall heat transfer, friction and fiber layer flow fraction exhibit a sudden decrease when S drops below a critical value, S_c. The critical stiffness number can be correlated as $S_c = C(H/L)^5(D/H)^2/(1-\phi)$, where C is a constant of order 0.4, H and D are the fiber length and diameter, L is the half-length of the solid wall, and ϕ is the porosity of the fiber layer.

INTRODUCTION

In this paper we document the fundamental friction and heat transfer characteristics of a surface covered by a layer of flexible fibers. The associated forced convection phenomenon has important applications in several fields, for example the enhancement of heat transfer [1], the control of the boundary layer [2, 3], heat and mass transfer from plant canopies [4], and biological oceanography, where suspension feeders and plant life are affected by the local flow behavior [5]. Our own interest in surfaces covered with flexible fibers was stimulated by questions of how to maximize the insulation effect of hair on mammals [6].

The model and flow configuration described in this paper have as their starting point the recent work on modelling convection through porous media in contact with fluids. In natural convection, the interaction between the flow through the porous medium and the flow of the pure fluid was documented by Poulikakos [7] and Sathe *et al.* [8]. Forced convection was documented by Vafai and Kim [1], Vafai and Thiyagaraja [9], and Poulikakos and Kazmierczak [10]. Relative to these studies and our own work on surfaces covered with hair [6], the present study focuses on two new aspects:

(1) the fibers that form the porous layer are flexible, and

(2) the external flow is originally perpendicular to the surface.

Aspect (1) deserves scrutiny because when the fibers are flexible the interaction between the porous medium and the external fluid is more complex than when the fibers are rigid. The flow that penetrates the porous layer can change the local properties (directional permeabilities) of the solid matrix, which in turn influence the flow.

Aspect (2) is a more realistic geometric feature of the flow past a finite-size body covered with fibers (e.g. the body of a mammal). The approaching fluid strikes the body perpendicularly, penetrates the fiber cover in the stagnation region, and later flows parallel to the surface and around the body.

THE PHYSICAL MODEL

The outer flow

To study the effects of fiber cover and fiber bending we selected the convection heat transfer configuration shown in Fig. 1. The flow enters the computational domain ($y = y_0$) with uniform velocity (U_∞) and temperature (T_c). The solid impermeable wall ($y = 0$) is maintained at a different temperature (T_h). The flow and temperature fields are symmetric about $x = 0$. In the region above the fibers ($y > H$), the flow is governed by the Navier–Stokes equations. The steady-state conservation of mass and momentum for incompressible flow are

$$\frac{\partial u}{\partial x} + \frac{\partial v}{\partial y} = 0 \tag{1}$$

$$u\frac{\partial u}{\partial x} + v\frac{\partial u}{\partial y} = -\frac{1}{\rho}\frac{\partial p}{\partial x} + \nu\left(\frac{\partial^2 u}{\partial x^2} + \frac{\partial^2 u}{\partial y^2}\right) \tag{2}$$

$$u\frac{\partial v}{\partial x} + v\frac{\partial v}{\partial y} = -\frac{1}{\rho}\frac{\partial p}{\partial y} + \nu\left(\frac{\partial^2 v}{\partial x^2} + \frac{\partial^2 v}{\partial y^2}\right) \tag{3}$$

† Author to whom correspondence should be addressed.

NOMENCLATURE

A_{ht}	heat transfer area in 1 rev [m^2]
$\tilde{A}_{ht}$	dimensionless heat transfer area
A_s	sum of fiber cross-section in 1 rev [m^2]
Bi	Biot number
c_p	specific heat at constant pressure [kJ kg^{-1} K^{-1}]
C	coefficient for the critical stiffness number correlation (51) (Fig. 14)
C_f	average skin friction coefficient
d_j	deflection of fiber segment [m]
D	fiber diameter [m]
E	modulus of elasticity [N m^{-2}]
F_x, F_y	force components [N]
h	heat transfer coefficient [W m^{-2} K^{-1}]
H	height of unbent fibers [m]
I	area moment of inertia [m^4]
k	fluid thermal conductivity [W m^{-1} K^{-1}]
k_s	fiber thermal conductivity [W m^{-1} K^{-1}]
$K_x, K_y, K_{xy}, K_\perp, K_\parallel$	permeabilities [m^2]
L	half-length of plane wall [m]
m	penetrating flow fraction
M_j	moment [N m]
n	number of fibers in 1 rev
N	number of fiber segments
Nu_L	average Nusselt number
p	pressure [N m^{-2}]
p_s	sum of wetted perimeters in 1 rev [m]
p_s	dimensionless sum of perimeters in 1 rev
P	dimensionless pressure
$\tilde{\mathbf{P}}_j$	position vector [m]
Pr	Prandtl number, ν/α
q''	heat flux [W m^{-2}]
rev	representative elementary volume
Re_L	Reynolds number
Re_p	porous medium Reynolds number
s	curvilinear coordinate [m]
S	stiffness number
S_c	critical stiffness number
T	temperature [K]
u, v	velocity components [m s^{-1}]
U, V	dimensionless velocity components
U_∞	approach velocity [m s^{-1}]
V_{rev}	volume of 1 rev [m^3]
W	width of plane wall [m]
x, y	coordinates [m]
X, Y	dimensionless coordinates.

Greek symbols

α	fluid thermal diffusivity [m^2 s^{-1}]
β	fiber angle (Fig. 2)
γ_c	critical fiber angle
γ_j	local fiber angle at node j
θ	dimensionless temperature
μ	viscosity [kg s^{-1} m^{-1}]
ν	kinematic viscosity [m^2 s^{-1}]
ρ	fluid density [kg m^{-3}]
$\tilde{\boldsymbol{\sigma}}$	stress vector [N m^{-2}]
ϕ	porosity.

Other symbols

$(\ )_b$	bare wall
$(\ )_c$	cold fluid
$(\ )_h$	hot wall
$(\ )_f$	fluid in the fiber layer
$(\ )_s$	solid matrix (fibers)
$(\ )''$	per unit area
$(\tilde{\ })$	dimensionless.

with the following boundary conditions in the plane of symmetry:

$$u = 0 \quad \frac{\partial v}{\partial x} = 0 \quad \text{at} \quad x = 0. \tag{4}$$

The pressure was set equal to an arbitrary constant ($p = 0$) at $x = L$ and $y = y_0$. The velocity components (u, v) were matched at the $y = H(x)$ interface with the volume-averaged velocity components (u_f, v_f) of the flow through the layer with fibers:

$$u = u_f \quad v = v_f \quad \text{at} \quad y = H(x). \tag{5}$$

The selection of velocity boundary conditions for the interface between a fluid and a porous medium saturated with the same fluid has generated considerable amount of work, which is reviewed in ref. [11]. According to the criteria developed by Vafai and Tien [12] we do not need to include the Brinkmann term in our porous flow model. It was shown by Vafai and Thiyagaraja [9], however, that one cannot match shear stresses across the interface without the inclusion of the Brinkman term. If one does not match shear stresses then one has to account for the possibility of a slip in the tangential velocity of the pure fluid at the interface, as was demonstrated by Beavers

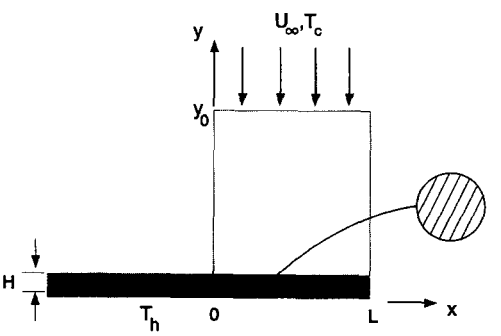

Fig. 1. Two-dimensional flow against a plane surface covered with fibers.

and Joseph [13]. In this problem the flow is mainly perpendicular to the surface; therefore the pressure field, which drives the flow within the porous layer, is not a strong function of the frictional drag at the surface. The pressure field is almost completely determined by the decrease in the vertical momentum of the approaching fluid. The result of this is that the problem is insensitive to the degree of slip at the fluid–porous interface. Numerical tests indicated that, if the no-slip condition is replaced with a free-slip condition, the resulting change is never greater than 2% in the frictional drag experienced at the wall, or in the heat transfer.

The velocity boundary conditions for the flow out of the computational domain ($x = L$) were $\partial^2 u/\partial x^2 = 0$ and $\partial^2 v/\partial x^2 = 0$. The insensitivity of numerical results to the specification of outflow boundary conditions has been demonstrated by numerous researchers (e.g. Huang and Vafai [2] and Vafai and Kim [1]). These conditions were compared with the zero stress conditions $p - 2\mu\,\partial u/\partial x = 0$ and $\partial v/\partial x = 0$ at $x = L$. The results for wall friction were the same for both sets of boundary conditions, but the zero stress condition caused velocity oscillations at the outlet.

The energy conservation equation and boundary conditions for the region with pure fluid are

$$u\frac{\partial T}{\partial x} + v\frac{\partial T}{\partial y} = \alpha\left(\frac{\partial^2 T}{\partial x^2} + \frac{\partial^2 T}{\partial y^2}\right) \tag{6}$$

$$\frac{\partial T}{\partial x} = 0 \quad \text{at} \quad x = 0 \quad T = T_c \quad \text{at} \quad y = y_0 \tag{7}$$

$$\frac{\partial^2 T}{\partial x^2} = 0 \quad \text{at} \quad x = L \quad T = T_f \quad \text{at} \quad y = H. \tag{8}$$

In the last of equations (8), the fluid temperature is matched to the porous medium temperature (T_f) at the interface between the two regions. Not shown is the energy continuity equation, in which the heat fluxes are matched across the $y = H(x)$ interface.

The layer with fibers

It was assumed that the flow in the region with fibers ($0 < y < H$) is in the Darcy regime. In a representative elementary volume (rev) [11] within this region, the solid matrix is a bundle of parallel equidistant fibers of diameter D. The volume-averaged flow direction almost never coincides with the local (rev) fiber direction because the outer flow is not uniform and the fibers can bend. When the flow through the fibers is perpendicular to the fiber direction, the permeability may be estimated using [14]

$$K_\perp = \frac{D^2}{125}\left[\frac{\phi^3}{(1-\phi)^2}\right]^{0.8}. \tag{9}$$

In the opposite extreme, when the flow is parallel to the fibers, the permeability has been correlated by Sparrow and Loeffler [15]:

$$\frac{K_\parallel}{D^2} = \frac{-\ln(1-\phi) - \phi - \phi^2/2}{16\phi(1-\phi)}. \tag{10}$$

This correlation is valid for $\phi > 0.8$ and for fibers arranged in an equilateral triangular array.

By analogy with the irreversible thermodynamics of heat conduction through an anisotropic medium [16], the Darcy flow equations for the general case where the flow is not parallel to the fibers ($\beta \neq 0$, Fig. 2) are

$$u_f = -\frac{K_x}{\mu}\frac{\partial p}{\partial x} - \frac{K_{xy}}{\mu}\frac{\partial p}{\partial y} \tag{11}$$

$$v_f = -\frac{K_{xy}}{\mu}\frac{\partial p}{\partial x} - \frac{K_y}{\mu}\frac{\partial p}{\partial y} \tag{12}$$

where

$$K_x = K_\perp \cos^2\beta + K_\parallel \sin^2\beta \tag{13}$$

$$K_y = K_\perp \sin^2\beta + K_\parallel \cos^2\beta \tag{14}$$

$$K_{xy} = (K_\parallel - K_\perp)\sin\beta\cos\beta. \tag{15}$$

When equations (11) and (12) are substituted into the mass conservation equation for the fiber region,

$$\frac{\partial u_f}{\partial x} + \frac{\partial v_f}{\partial y} = 0. \tag{16}$$

the result is a partial differential equation for the pressure field:

$$\left(\frac{\partial K_x}{\partial x} + \frac{\partial K_{xy}}{\partial y}\right)\frac{\partial p}{\partial x} + K_x\frac{\partial^2 p}{\partial x^2} + \left(\frac{\partial K_{xy}}{\partial x} + \frac{\partial K_y}{\partial y}\right)\frac{\partial p}{\partial y} + K_y\frac{\partial^2 p}{\partial y^2} + 2K_{xy}\frac{\partial^2 p}{\partial x\,\partial y} = 0. \tag{17}$$

This equation allows for the fact that the permeabilities vary from one rev to another inside the fiber region. The boundary conditions for equation (17) are

$$\frac{\partial p}{\partial x} = 0 \quad \text{at} \quad x = 0 \tag{18}$$

$$\frac{\partial p}{\partial y} = 0 \quad \text{at} \quad y = 0 \tag{19}$$

$$p = p(H) \quad \text{at} \quad x = L \tag{20}$$

and the condition that p is continuous across the $y = H$ interface, which is the fourth boundary condition needed. The pressure $p(H)$ is provided by the solution to the pure fluid part of the flow field. The constant pressure condition (20) is the better of two conditions that were tried at $x = L$. The difficulty associated with equation (20) is that it forces $v_f = 0$ at $x = L$. This feature causes a sharp change in the vertical velocity component across the $y = H$ interface is Re_L is large. The alternative to equation (20) was $\partial p/\partial x =$ constant at $x = L$. This was superior in cases where the fibers did not bend, but when the fibers bent a region of highly negative pressure formed around $x = L$ and $y = 0$. This was not acceptable given that

$p = 0$ was the ambient pressure, so the constant-p condition (20) was adopted. It must be said that either condition, constant p or constant $\partial p/\partial x$, led to similar results for friction and heat transfer over the wall region $0 < x < L$: the relative error between the two sets of results decreased from 10% at $L/H = 2$ to less than 1% at $L/H = 5$. In these L/H ratios, H is the original height of the fiber layer before it is deformed by the flow, or simply H evaluated at $x = 0$ (Fig. 13).

We now turn our attention to the thermal aspects of the model. In each rev, the temperature is represented by two values, the temperature of the solid (the fibers, T_s) and the temperature of the interstitial fluid (T_f). The conduction of heat along the fiber is described by the unidirectional fin conduction model:

$$k_s \frac{\partial^2 T_s}{\partial s^2} + h \frac{p_s}{A_s}(T_f - T_s) = 0 \tag{21}$$

where s is the curvilinear coordinate measured along the fiber ($s = 0$ is the base). In each rev cut perpendicular to the fiber direction, the sum of all the fiber wetted perimeters is p_s, and the sum of all the fiber cross-sections is A_s. For each local angle of fiber inclination β, the ratio p_s/A_s is a constant dictated by the fiber diameter and the fiber density (or the porosity ϕ along the $y = 0$ wall, where all the fibers are perpendicular to the wall).

The equation for the conservation of energy in the interstitial fluid is

$$\frac{u_f}{\phi}\frac{\partial T_f}{\partial x} + \frac{v_f}{\phi}\frac{\partial T_f}{\partial y} = \alpha\left(\frac{\partial^2 T_f}{\partial x^2} + \frac{\partial^2 T_f}{\partial y^2}\right) + \frac{h}{\rho c_p}\frac{A_{ht}}{\phi V_{rev}}(T_s - T_f) \tag{22}$$

where V_{rev} is the rev volume, and $A_{ht}/(\phi V_{rev})$ is the ratio of the total fiber–fluid contact area present in the rev, divided by the volume inhabited by fluid in the rev. The thermal diffusivity α refers to the fluid alone, $\alpha = k/(\rho c_p)$. The heat transfer coefficient appearing in equations (21) and (22) was estimated based on the low Reynolds number correlation developed in ref. [14], where it was found that in the range $0° < \beta < 60°$ the effect of β on h is negligible:

$$h = (8.46 - 6.8\phi)\frac{k}{D}\left(\frac{U_\infty D}{\alpha}\right)^{0.18}. \tag{23}$$

This correlation is valid in the range $0.9 \leqslant \phi \leqslant 0.95$, $1 \leqslant U_\infty D/\alpha \leqslant 30$, and $0.72 \leqslant Pr \leqslant 100$. The boundary conditions for equations (21) and (22) are

$$T_s = T_f = T_h \quad \text{at} \quad y = 0 \tag{24}$$

$$\frac{\partial T_f}{\partial x} = 0 \quad \text{at} \quad x = 0 \quad \text{and} \quad x = L \tag{25}$$

$$T_f = T \quad \text{at} \quad y = H \tag{26}$$

$$\frac{\partial T_s}{\partial s} = 0 \quad \text{at the fiber end.} \tag{27}$$

Worth noting are: the outflow condition $\partial T_f/\partial x = 0$ at $x = L$, which is commonly used in numerical studies of convection in porous media with permeable walls [17–20], the fluid temperature continuity across the $y = H$ interface [equation (26)] and the assumption that each fiber is slender enough so that the heat transfer through its tip can be neglected [equation (27)].

The equations and boundary conditions described until now were nondimensionalized by defining

$$(U, U_f) = \frac{(u, u_f)}{U_\infty} \quad (V, V_f) = (v, v_f)\frac{H}{U_\infty L} \tag{28}$$

$$X = \frac{x}{L} \quad Y = \frac{y}{H} \quad P = \frac{p}{\rho U_\infty^2} \tag{29}$$

$$(\theta, \theta_f, \theta_s) = \frac{(T, T_f, T_s) - T_c}{T_h - T_c}. \tag{30}$$

For brevity, we omit the dimensionless equations and boundary conditions, and note that they contain the following dimensionless groups:

$$Re_L = \frac{U_\infty L}{\nu} \quad Pr = \frac{\nu}{\alpha} \quad A = \frac{L}{H} \tag{31}$$

$$Nu_L = \frac{hL}{k} \quad \tilde{A}_{ht} = \frac{A_{ht}L}{\phi V_{rev}} \quad Bi = \frac{hL}{k_s} \quad \tilde{p}_s = \frac{p_s L}{A_s}. \tag{32}$$

The fiber shape

The third component of the model contains the equations needed for calculating the shape of the fibers. This component is based on the observation that in Darcy flow the pressure gradient in the fluid is balanced by the forces exerted on the solid matrix. We assume that the fibers do not touch, i.e. that each fiber acts independently of all other fibers. Consider a small volume $\mathrm{d}x\,\mathrm{d}y\,W$ that contains at least 1 rev, where $W \gg L$ is the dimension perpendicular to the plane of Fig. 1. The components of the total force experienced by the solid parts (fiber segments) found in this volume are

$$F_x = -\frac{\partial p}{\partial x}\mathrm{d}x\,\mathrm{d}y\,W \quad F_y = -\frac{\partial p}{\partial y}\mathrm{d}x\,\mathrm{d}y\,W. \tag{33}$$

The number of fibers that pass through this volume is

$$n = (\cos\beta\,\mathrm{d}x + \sin\beta\,\mathrm{d}y)\,W\frac{1-\phi}{\pi D^2/4} \tag{34}$$

where $(1-\phi)/(\pi D^2/4)$ is the fiber density (number/area) in the plane perpendicular to the local fiber direction. Dividing equations (33) by n yields the components of the local load experienced by a single fiber. These forces can be arranged into a stress vector $\tilde{\boldsymbol{\sigma}}$: the normal and tangent forces exerted at a certain point(s) on the fiber are obtained by performing the scalar product between $\tilde{\boldsymbol{\sigma}}$ and the unit normal and unit tangent vectors.

Each fiber was divided into many small segments (N), typically $N = 50$. The forces were modelled as acting on the ends of each segment. Each small

segment, therefore, behaved as a beam undergoing small deflection. The normal and tangential forces were transferred down the fiber according to the equations

$$FN_j = \tilde{\sigma}_j \cdot \hat{\mathbf{N}}_j + (\hat{\mathbf{N}}_j \cdot \hat{\mathbf{N}}_{j+1}) FN_{j+1} + (\hat{\mathbf{N}}_j \cdot \hat{\mathbf{T}}_{j+1}) FT_{j+1} \tag{35}$$

$$FT_j = \tilde{\sigma}_j \cdot \hat{\mathbf{T}}_j + (\hat{\mathbf{T}}_j \cdot \hat{\mathbf{T}}_{j+1}) FT_{j+1} + (\hat{\mathbf{T}}_j \cdot \hat{\mathbf{N}}_{j+1}) FN_{j+1} \tag{36}$$

where the unit normal $\hat{\mathbf{N}}$ is defined as $(\cos\beta_j, -\sin\beta_j)$ and the unit tangent $\hat{\mathbf{T}}$ is defined as $(\sin\beta_j, \cos\beta_j)$. Following the method of Knight and Barret [21], these forces can be used to calculate the deflection of each fiber segment, and thereby build up the shape of the entire fiber.

Figure 2 illustrates the node placement relative to one fiber segment, where γ_j is the local fiber angle at node j. The angle β associated with the jth segment is the angle between the y-axis and the straight line segment joining the j and $j+1$ nodes. The fiber segments that join the nodes are not necessarily straight. The mass stations that would be present in a time-dependent beam analysis are not necessary because in this study we are concerned with the steady state. Only the elastic elements are represented:

$$\gamma_j = \Delta\gamma_j + \gamma_{j-1} \tag{37}$$

$$\Delta\gamma_j = \frac{M_j \Delta s}{EI} + \frac{FN_j (\Delta s)^2}{2EI} \tag{38}$$

$$M_j = M_{j+1} + \Delta s FN_{j+1}. \tag{39}$$

In equations (38) and (39) Δs is the length of the fiber segment, E is the elastic modulus, $I = \pi D^4/64$ is the area moment of inertia, and M_j is the bending moment at node j. Equations (35)–(39) and the end conditions $\gamma = 0$ at $s = 0$, and $M_N = 0$ at the free end are sufficient for calculating all the γ_js. To calculate the position of each node, we calculate the end deflection of each segment:

$$d_j = \frac{M_j (\Delta s)^2}{2EI} + \frac{FN_j (\Delta s)^3}{3EI}. \tag{40}$$

The position vector for node j is

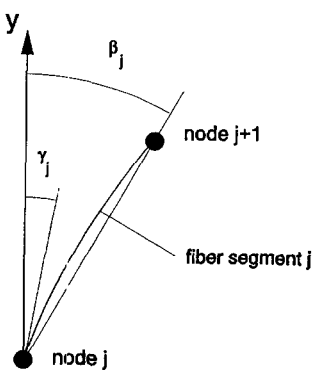

Fig. 2. The deflection of one fiber segment.

$$\tilde{\mathbf{P}}_j = \Delta s \hat{\mathbf{T}}(\gamma_{j-1}) + d_j \hat{\mathbf{N}}(\gamma_{j-1}) \tag{41}$$

where $\hat{\mathbf{T}}$ and $\hat{\mathbf{N}}$ are the tangent and normal vectors calculated in terms of the angles γ_j rather than β_j. The local fiber angle can be calculated for each segment:

$$\beta_{j-1} = \tan^{-1}\left(\frac{\tilde{\mathbf{P}}_{jy} - \tilde{\mathbf{P}}_{(j-1)y}}{\tilde{\mathbf{P}}_{jx} - \tilde{\mathbf{P}}_{(j-1)x}}\right) \tag{42}$$

where $\tilde{\mathbf{P}}_{jy}$ refers to the y-position of the jth node, and $\tilde{\mathbf{P}}_{jx}$ refers to the x-position of the jth node. These equations were also nondimensionalized, and this brought to light a new dimensionless group that describes the relative stiffness of the fibers:

$$S = \frac{EI}{\rho U_\infty^2 L^4}. \tag{43}$$

THE NUMERICAL METHOD

The equations governing the flow in the pure fluid region were solved using finite differences and ADI. The pressure field was solved in order to force the conservation of mass using the auxiliary potential method [22]. The grid in the pure fluid region was uniform in x, but variable in y, so that a large number of grid points could be put in the boundary layer near the porous interface (Fig. 3). A shearing transformation was used to map the nonrectangular physical domain, which occurs when the fibers bend, onto a rectangular computational domain. The robustness of the solver was increased dramatically by including an artificial viscosity that was non-zero only in a region with positive v. There is no artificial viscosity in the final results because all the solutions are characterized by negative v velocities.

The pressure field in the layer with fibers was also solved using finite differences and ADI. The grid in the porous region was uniform in x and y in computational space (Fig. 3). Another shearing transformation was used to map the irregular porous domain onto a rectangular computational space.

The equations for the fluid temperature were solved using ADI on a non-sheared grid, with the same grid point placement as the fluid equations when the fibers were unbent. The temperature in the solid was determined using time stepping with the trapezoidal rule until convergence was reached.

The pure fluid velocity solution was iterated until the relative error (maximum change in velocity divided by the time step) was less than 0.1. The auxiliary potential solver was then iterated until its relative error became less than 0.001. Then the porous pressure field was solved, using the new pressure boundary conditions provided by the auxiliary potential solution. The porous pressure field was iterated until its relative error was less than 0.0001. When the fibers were bent, convergence testing indicated that a relative error of 10^{-5} was necessary.

The cycle continued until the average value of the auxiliary potential function was less than 0.001 (which

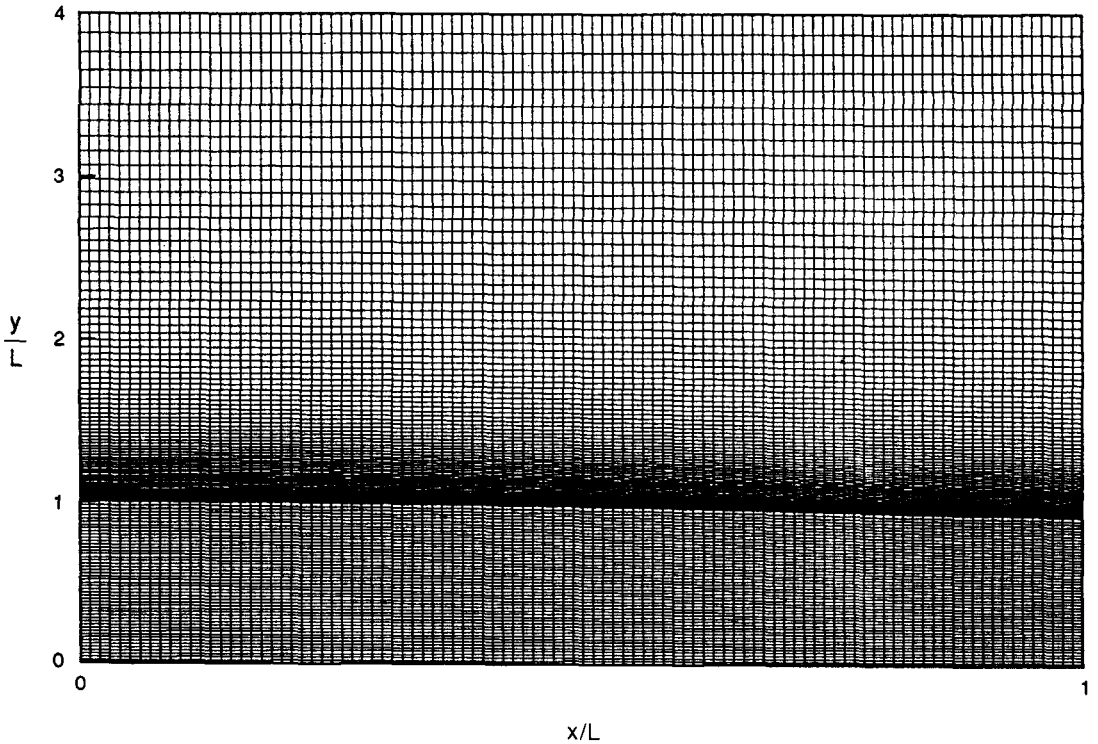

Fig. 3. Example of the grid used ($Re_L = 1000$, $L/H = 2$, $\phi = 0.9$, $H/D = 20$).

indicates that continuity is being satisfied). All of these tolerances were determined doing convergence testing. In all cases, dividing any of the above convergence criteria by 2 resulted in a less than 1% change in the calculated friction force on the $y = 0$ surface. Two additional accuracy criteria that were met are that global mass conservation must be satisfied to better than 1%, and that mass conservation within the porous layer must be satisfied within 1%. The latter criterion was relaxed to 3% when the fibers underwent significant deformation. It was also found that setting $y_0 = 4L$ made the solution insensitive to further increases in the height of the computational domain.

Similarly, the fluid temperature was advanced by one time step (the size of which was determined by stability criteria) and then the solid temperature was iterated until convergence was reached, and the fluid temperature was advanced again. The system generally conserved energy to within 1% if the relative fluid temperature error was less than 0.001. In cases where the total conservation of energy was not satisfied to within 3%, error bars are attached to the plotted results.

Grid refinement tests were performed. The final grid was chosen such that further grid doubling in any direction resulted in a less than 1% change in the calculated surface friction. The final grid for $Re_L = 500$ was 101 points in x for both the porous and non-porous regions, 81 grid points in y for the pure fluid region, and 50 grid points in y for the porous region. An example of the mesh used for a solution in which the fibers are bent is illustrated in Fig. 3: note that the height of the porous layer decreases as x increases, because the fibers bend.

SURFACE WITH INFLEXIBLE FIBERS

Before examining the effect of fiber bending on friction and heat transfer, it is necessary to understand the convection mechanism when the fibers do not bend. How stiff the fibers (or how large S) must be in this limit is one of the results presented in the next section.

The independent parameters in the system are Re_L, Pr, the porosity of the fiber layer ϕ, the aspect ratio L/H, the fiber height to fiber diameter ratio H/D, and the ratio of solid to fluid conductivities k_s/k. In this study the fluid is assumed to be air, $Pr = 0.72$. If the fibers are hairs in air then $k_s/k \cong 10$. We considered several Re_L values between 500 and 2000, several porosities between 0.9 and 0.95, H/D ratios of 20 and 50, and aspect ratios $L/H = 1$–5. The results are presented in terms of overall quantities: the average skin friction coefficient

$$C_f = \frac{\int_0^L F''_x \, dx}{\frac{1}{2}\rho U_\infty^2 L} \quad \text{where} \quad F''_x = \int_0^H -\frac{\partial p}{\partial x} dy \quad (44)$$

and the average Nusselt number

$$Nu_L = \frac{hL}{k} \quad \text{where} \quad h = \frac{\int_0^L q''|_{y=0} \, dx}{(T_h - T_c)L}. \quad (45)$$

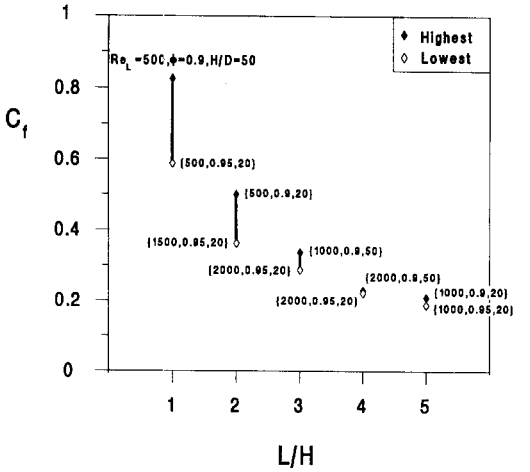

Fig. 4. The average skin friction coefficient for a wall with inflexible fibers.

Figure 4 shows that the average skin friction coefficient depends mainly on L/H, and is roughly inversely proportional to L/H. The insensitivity of C_f to changes in Re_L, ϕ and H/D is particularly evident when $L/H > 2$, although minor even when $L/H < 2$. The effect of increasing H/D is to increase C_f, while the effect of increasing ϕ is to decrease C_f.

The results for heat transfer are more complicated. Figure 5(a) shows the effect of the porosity and the Reynolds number: the total heat transfer rate increases with both ϕ and Re_L. More interesting is the alternative shown in Fig. 5(b), where $Nu_L/Nu_{L,b}$ is the ratio between the actual Nu_L value [Fig. 5(a)] and the value calculated for the same Re_L in the limit where the wall surface is bare (no fibers, or $L/H \to \infty$). Interesting is how the ratio $Nu_L/Nu_{L,b}$ compares with 1. Below a critical porosity [roughly 0.94 in Fig. 5(b)], the fibers provide an insulation effect, and $Nu_L < Nu_{L,b}$. Above the critical porosity, the permeability of the porous layer is sufficiently high, and the cold flow entering from above is sufficiently strong, that the fibers act as fins surrounded by cold fluid. In this regime the fibers augment the heat transfer from the wall, $Nu_L > Nu_{L,b}$. These two extremes, i.e. the fact that hair-like fibers provide insulation in some cases and augmentation in others, confirm the main point of the theoretical work or surfaces covered with hair [6]. That a porous layer can cause the augmentation of heat transfer was also found by Vafai and Kim [1] for flow parallel to a wall.

The effect of Re_L on the heat transfer is illustrated in greater detail in Fig. 6. The heat transfer through the wall with fibers increases almost proportionally with Re_L. This increase is steeper than when the wall is bare, because $Nu_L/Nu_{L,b}$ also increases with L. In conclusion, the faster flow (higher Re_L) removes more heat because of two effects: (1) cold fluid comes closer to the wall, as in the case of a bare wall; and (2) the fibers provide a finning effect.

Figure 7 shows the end result of a search [14] for a

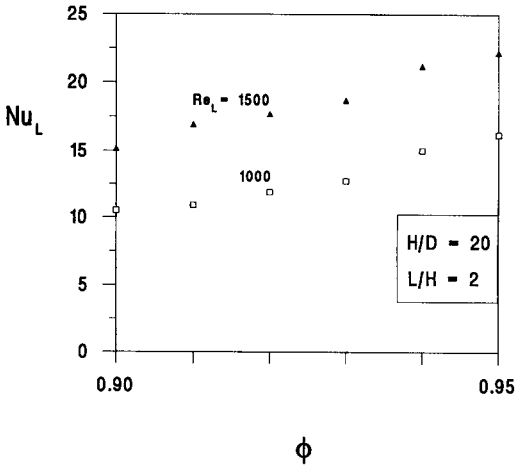

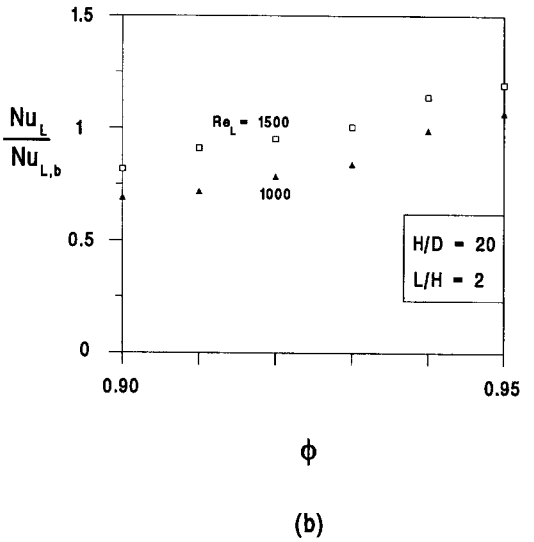

Fig. 5. The average Nusselt number for a wall with inflexible fibers.

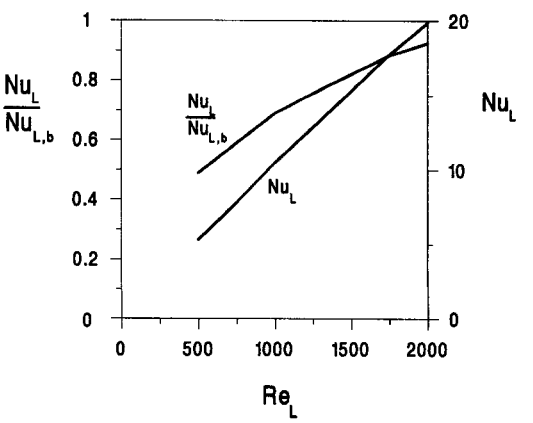

Fig. 6. The effect of Reynolds number on heat transfer when the fibers do not bend.

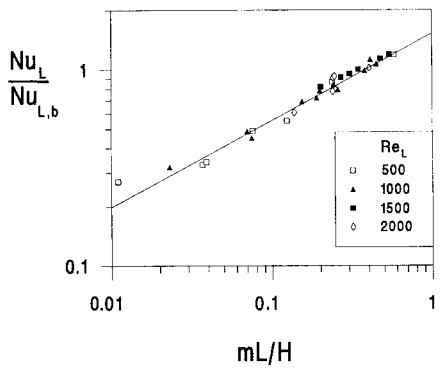

Fig. 7. Heat transfer correlation for a wall with inflexible fibers.

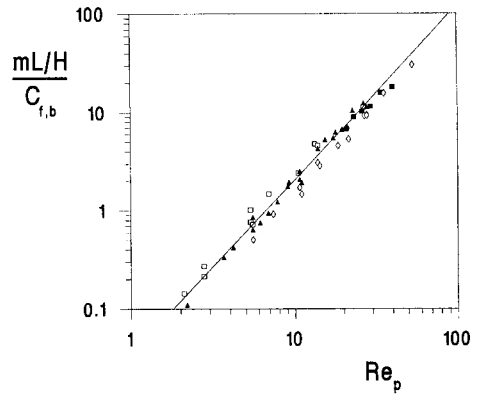

Fig. 8. Correlation for the fraction of the external flow that penetrates into the layer with fibers.

way to correlate the numerical heat transfer results for surfaces covered with stiff fibers. The parameter chosen on the abscissa is mL/H, where m is the fraction of the total external flow ($U_\infty L$) that penetrates into the fiber layer:

$$m = \frac{1}{U_\infty L}\int_0^L (-v)_{y=H}\,\mathrm{d}x. \tag{46}$$

The numerical $Nu_L/Nu_{L,b}$ data correlated in Fig. 7 cover the range $0.9 \leqslant \phi \leqslant 0.95$, $500 \leqslant Re_L \leqslant 2000$, $H/D = 20$ and 50, and $L/H = 1$–5. The line

$$\frac{Nu_L}{Nu_{L,b}} = 1.58\left(m\frac{L}{H}\right)^{0.4} - 0.051 \tag{47}$$

approximates the data with a mean error of 5.2%.

It is to be expected that equation (47) will fail in the limit $mL/H \to 0$, where there is no flow through the fiber layer. In that limit the Nusselt number reaches a minimum value, $Nu_{L,min}$, which can be evaluated based on the parallel thermal resistance model (trapped fluid in parallel with fibers)

$$Nu_{L,min} = \left(Nu_{L,b}^{-1} + \left\{\frac{L}{H}\left[\phi + \frac{k_s}{k}(1-\phi)\right]\right\}^{-1}\right)^{-1}. \tag{48}$$

If the Nu_L value calculated with equation (47) is less than $Nu_{L,min}$, then the correct value is $Nu_{L,min}$ given by equation (48). To illustrate this observation, consider the leftmost datum (a square) plotted in Fig. 7: that point corresponds to $\phi = 0.9$, $L/H = 2$, $H/D = 50$ and $Re_L = 500$, for which equation (48) yields $Nu_{L,min} = 2.8$. This means that $Nu_{L,min}/Nu_{L,b} = 0.26$, which is greater than the ratio found using equation (47), $Nu_L/Nu_{L,b} = 0.2$. The actual Nu_L value determined numerically is 2.9, which is very close to $Nu_{L,min} = 2.8$ given by equation (48).

To calculate the heat transfer based on the correlation (47) or Fig. 7, we need a way to predict mL/H. Figure 8 shows the correlation

$$\frac{mL/H}{C_{f,b}} = 0.0476Re_p^{1.7} - 0.029 \tag{49}$$

where $C_{f,b}$ is the average skin friction coefficient for the bare wall. The mean error between the data and equation (49) is 18.6%. The abscissa parameter is the Reynolds number used in convection through porous media [23], namely $Re_p = U_\infty K_\perp^{1/2}/\nu$.

The skin friction and heat transfer correlations for the bare-wall limit are presented in Fig. 9. The dashed line shows an empirical correlation developed by Sparrow *et al.* [24] from experiments measuring mass transfer from a plate $2\frac{1}{2}$ times as wide as it was long, which was subjected to incident flow at angles from 25° to 90°. The form of their correlation is $Nu_L = 0.939Re_{L^*}^{1/2}\,Pr^{1/3}\,Re_L$, where $L^* = 4A/C$, A is the plate area, and C is the plate circumference. Sparrow *et al.* found that by using Re_{L^*} in the correlation they eliminated almost entirely the geometric dependence of Nu_L. Their experiments showed, however, a small geometric dependence for the leading factor (0.939 above): this factor increases as the width of the plate increases. In their experiments, the Nu_L increase from a narrow plate (width/length = 0.4) to the wider plate was 9%. This change is consistent with the 12% difference between the dashed line and our Nu_L results (the solid line), because our results are for a plate of infinite width.

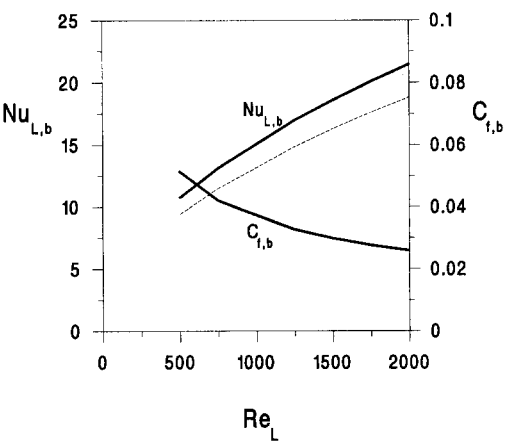

Fig. 9. Skin friction and heat transfer results for the bare wall limit ($Pr = 0.72$).

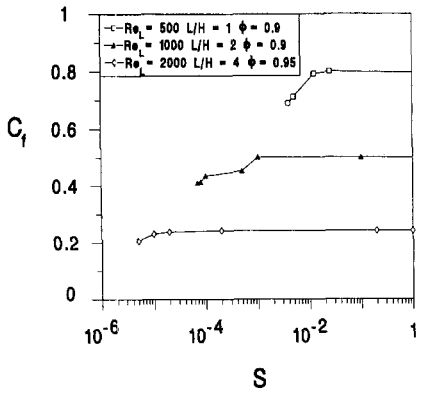

Fig. 10. The effect of fiber stiffness on skin friction.

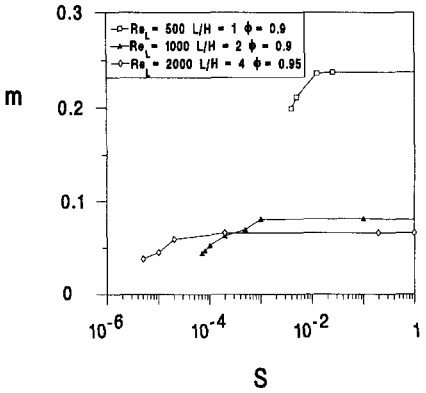

Fig. 12. The effect of fiber stiffness on flow penetration into the fiber layer.

THE EFFECT OF FIBER BENDING

We examined the effect of fiber bending by varying the stiffness parameter S. We considered three cases:

$$(Re_L = 500, L/H = 1, \phi = 0.9, H/D = 20),$$

$$(Re_L = 1000, L/H = 2, \phi = 0.9, H/D = 20)$$

and

$$(Re_L = 2000, L/H = 4, \phi = 0.95, H/D = 20).$$

The selected ϕ and H/D values are such that a significant fraction of the external flow penetrates into the fiber layer. The characteristics of the fiber cover on the $L/H = 1$ and $L/H = 2$ surfaces are identical, so they correspond physically to two surfaces with identical covering, but with different lengths, L and $L/2$, respectively. The maximum fiber bending calculated was $\beta = 20°$ for $L/H = 1$, $\beta = 40°$ for $L/H = 2$ and $\beta = 38°$ for $L/H = 4$.

Figures 10–12 illustrate the effect of fiber bending on the skin friction, heat transfer and flow penetration into the fibers. In the geometries considered the transition from 'no S effect' to 'substantial S effect' is fairly abrupt. More flexible fibers (lower S values) mean smaller C_f, Nu_L and m values.

Figure 10 illustrates the effect of fiber bending on skin friction. For the three surfaces the effect is significant. The decrease in C_f from the case of no bending to the maximum bending calculated is about 15% in all cases (specifically, 14, 18 and 15% for $L/H = 1$, 2 and 4, respectively). Figure 11 shows, however, that the effect of fiber bending on Nu_L is small. The total decrease in Nu_L is 5, 8 and 6% for the three surfaces. From the result for surfaces with inflexible fibers one might conclude that the magnitude of the penetrating flow m must also be insensitive to the fiber bending. Examination of Fig. 12, however, shows that this is not the case.

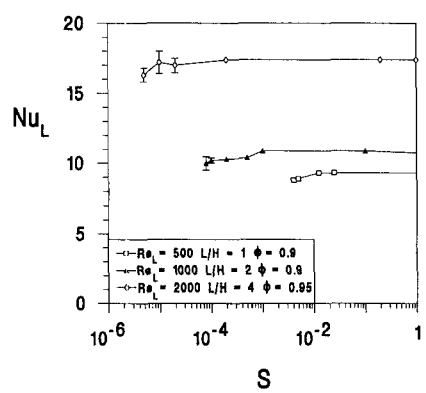

Fig. 11. The effect of fiber stiffness on heat transfer.

The effect of fiber bending on the flow penetrating the fiber layer (m) is shown in Fig. 12. The effect is quite large: 45% for $L/H = 2$ and 43% for $L/H = 4$. According to the relationship developed for predicting Nu_L based on m for a surface covered with inflexible fibers [equation (47)] a 45% decrease in m should result in about a 21% decrease in Nu_L; but, as was shown in Fig. 11, Nu_L actually decreases by only 5–8% while m decreases by 43–45%. This suggests that, while less flow enters the fiber layer as a whole, the flow must be penetrating to the warm surface at a rate roughly independent of fiber bending.

A possible explanation for this is that when the fibers bend they orient themselves in a direction closer to perpendicular to the downward coming flow: this decreases the layer's permeability. At the same time, however, the spreading of the fibers causes an increase in porosity, which causes an increase in permeability. The spreading tends to occur near $x = 0$, and the maximum fiber bending occurs near $x = L$ (Fig. 13). This results in a deflection of the $x = L$ fluid away from the fiber layer, but allows fluid into the small-x region at the same (or even a higher) rate as the rate that occurs when the fibers do not bend.

Figure 13 illustrates the progressive bending of the fibers as the stiffness S decreases for the $L/H = 4$ surface. Each 'fiber' line drawn on the fiber surface represents many actual fibers. The number represented per line depends upon ϕ, and H/D. It is clear from the figure that the region near $x = L$ is much less permeable to downward flow because of the fiber angle and decreased porosity. The minimum porosity for the $L/H = 4$ surface was $\phi \cong 0.935$, which corresponds to $\phi = 0.95$ when the fibers are straight.

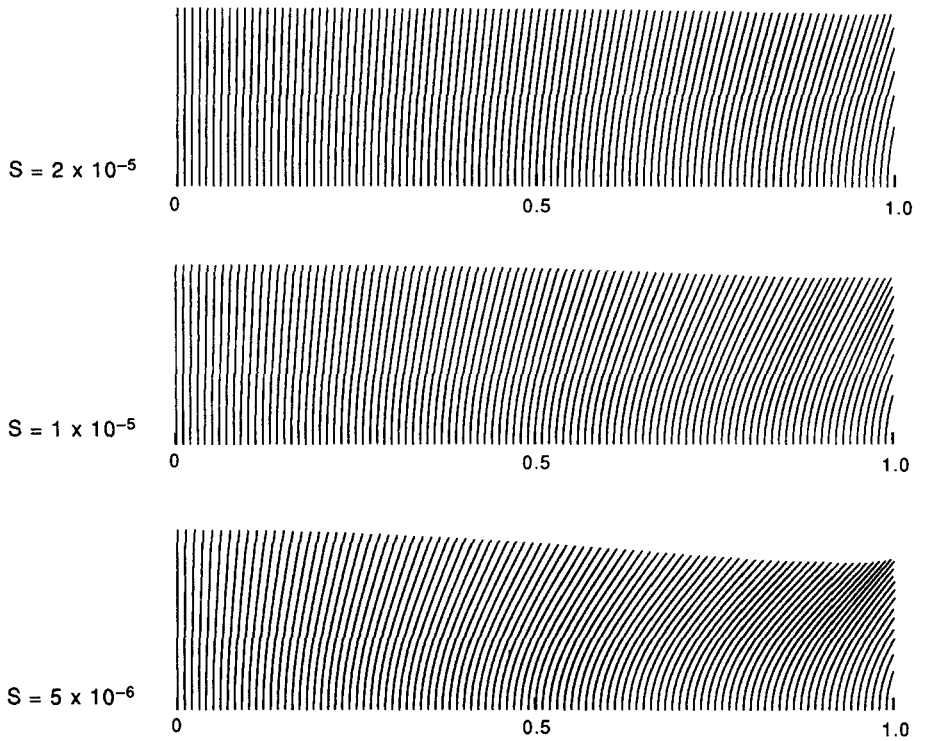

Fig. 13. The effect of stiffness on the fiber shape ($Re_L = 200$, $L/H = 4$, $\phi = 0.95$, $H/D = 20$).

To summarize, Figs. 10–13 show that the bending of the fibers begins to have an effect when the stiffness number S drops below a certain, critical level. We recorded this effect quantitatively, by first defining the critical stiffness number S_c as the S value where m drops to 90% of its value for inflexible fibers:

$$m(S = S_c) = 0.9m(S \to \infty). \tag{50}$$

We then determined numerically the $m(S)$ dependence for a series of 12 cases, of which only three are illustrated in Fig. 10. The resulting S_c values can be correlated as

$$S_c = \frac{C}{1-\phi}\left(\frac{H}{L}\right)^5\left(\frac{D}{H}\right)^2 \tag{51}$$

for which the C coefficient is reported in Fig. 14. The analytical form of equation (51) was derived based on equation (38) and the hypothesis that the critical stiffness S_c corresponds to a critical fiber angle γ_c. Figure 14 shows that in the parametric domain considered the C coefficient does not depend systematically on Re_L. The most we can say is that C is a number of order 0.4. That a correlation of type (51) should hold is suggested also by Fig. 4, which implies that the dimensionless pressure field is largely insensitive to Re_L.

Setting $C = 0.4$ in equation (51) allows us to predict S_c to within a factor of 2 for all the cases tested. We expect this relationship to hold for high Re_L flows where the viscous effects on the pressure field will continue to be negligible. Equation (51) should break down at sufficiently low Re_L values, because in that direction viscous effects become important. Low Re_L flows, however, are also characterized by little or no penetrating flow in the fiber layer, which makes these flows of considerably less interest.

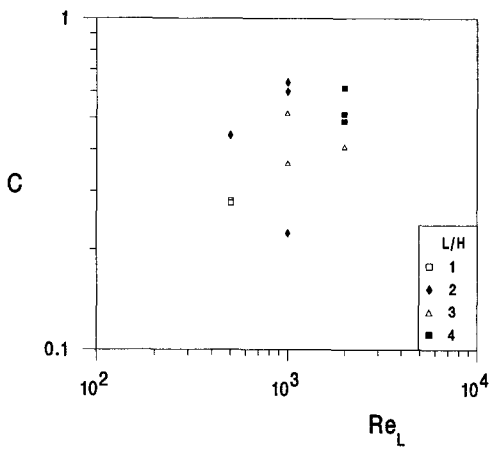

Fig. 14. The C coefficient for the critical stiffness correlation (51) ($\phi = 0.9$–0.95, $H/D = 20$ and 50).

CONCLUDING REMARKS

In this paper we investigated the interaction between a solid surface and an external flow when the solid is covered with a layer of fibers. The objective was to document the way in which the fiber layer properties affect the overall heat transfer and friction characteristics of the surface.

In the first part of this study we considered the limit

in which the fibers are inflexible. The results presented in Figs. 4–9 and in the text show that the fiber layer can alter significantly the wall characteristics, especially the overall heat transfer. A peculiar effect is due to the porosity: at porosities lower than a critical value, the fiber cover acts as an insulation, while at higher porosities the fibers augment the heat transfer [Fig. 5(b)]. We showed that the effect of the fiber cover can be correlated in terms of the flow fraction that penetrates into the fibers (Figs. 7 and 8).

In the second part we examined the bending of the fibers, as they interact with the flow that penetrates the fiber layer. The fiber bending is governed by the nondimensional stiffness number S. We found that, when S decreases below a critical value S_c, there is a sudden drop in wall friction, heat transfer and penetrating flow fraction (Figs. 10–12). The least sensitive to changes in S is the overall heat transfer rate (Fig. 11). We showed that the critical stiffness number S_c values determined numerically can be correlated [cf. equation (51) and Fig. 14].

Acknowledgement—This work was sponsored by the Air Force Office of Scientific Research under the guidance of Major Dan Fant.

REFERENCES

1. K. Vafai and S. J. Kim, Analysis of surface enhancement by a porous substrate, *J. Heat Transfer* **112,** 700–706 (1990).
2. P. C. Huang and K. Vafai, Flow and heat transfer control over an external surface using a porous block array arrangement, *Int. J. Heat Mass Transfer* **36,** 4019–4032 (1993).
3. P. C. Huang and K. Vafai, Passive alteration and control of convective heat transfer utilizing alternate porous cavity-block wafers, *Int. J. Heat Fluid Flow* **15,** 48–61 (1994).
4. D. A. deVries and N. H. Afgan, *Heat and Mass Transfer in the Biosphere Part* 1: *Transfer Processes in the Plant Environment.* Scripta, Washington, DC (1975).
5. A. R. M. Nowell and P. A. Jumars, Flow environments of aquatic benthos, *A. Rev. Ecol. Systems* **15,** 303–328 (1984).
6. A. Bejan, Theory of heat transfer from a surface covered with hair, *J. Heat Transfer* **112,** 662–667 (1990).
7. D. Poulikakos, Buoyancy-driven convection in a horizontal fluid layer extending over a porous substrate, *Phys. Fluids* **29,** 3949–3957 (1986).
8. S. B. Sathe, W. Q. Lin and T. W. Tong, Natural convection in enclosures containing an insulation with a permeable fluid–porous interface, *Int. J. Heat Fluid Flow* **9,** 389–395 (1988).
9. K. Vafai and R. Thiyagaraja, Analysis of flow and heat transfer at the interface region of a porous medium, *Int. J. Heat Mass Transfer* **30,** 1391–1405 (1987).
10. D. Poulikakos and M. Kazmierczak, Forced convection in a duct partially filled with a porous material, *J. Heat Transfer* **109,** 653–662 (1987).
11. D. A. Nield and A. Bejan, *Convection in Porous Media.* Springer Verlag, New York (1992).
12. K. Vafai and C. L. Tien, Boundary and inertia effects on flow and heat transfer in porous media. *Int. J. Heat Mass Transfer* **24,** 195–202 (1981).
13. G. S. Beavers and D. D. Joseph, Boundary conditions at a naturally permeable wall, *J. Fluid Mech.* **30,** 197–207 (1967).
14. A. J. Fowler, Fundamental topics in heat transfer through deformable two-phase media, Ph.D. thesis, Duke University (1993).
15. E. M. Sparrow and A. L. Loeffler, Jr., Longitudinal laminar flow between cylinders arranged in a regular array, *A.I.Ch.E. Jl* **5,** 325–330 (1959).
16. A. Bejan, *Advanced Engineering Thermodynamics*, pp. 696–706. Wiley, New York (1988).
17. V. Hlavacek and J. Votruba, Steady-state operation of fixed-bed reactors and monolithic structures. In *Chemical Reactor Theory, a Review* (Edited by L. Lapidus and N. R. Amundson), pp. 314–404. Prentice-Hall, Englewood Cliffs, NJ (1977).
18. T. Handa, M. Morita, O. Sugawa, T. Ishii and K. Hayashi, Computer simulation of the spontaneous combustion of coal storage, *Fire Sci. Technol.* **3,** 13–24 (1983).
19. D. Schmal, J. H. Duyzer and J. van Heuven, A model for the spontaneous heating of coal, *Fuel* **64,** 963–972 (1985).
20. J. E. Gatica, H. J. Viljoen and V. Hlavacek, Interaction between chemical reaction and natural convection in porous media, *Chem. Engng Sci.* **44,** 1853–1870 (1989).
21. J. D. Knight and L. E. Barrett, The effect of flexible couplings on the undamped lateral vibrations of rotor-bearing systems, Report No. UVA/464761/MAE80/170, University of Virginia, Charlottesville, VA (1980).
22. C. A. J. Fletcher, *Computational Techniques for Fluid Dynamics*, Vol. 2, pp. 360–362. Springer-Verlag, New York (1991).
23. P. Cheng, Heat transfer in geothermal systems, *Adv. Heat Transfer* **14,** 1–105 (1978).
24. E. M. Sparrow, J. W. Ramsey and E. A. Mass, Effect of finite width on heat transfer and fluid flow about an inclined rectangular plate, *J. Heat Transfer* **101,** 199–204 (1979).